ACS APPLIED MATERIALS & INTERFACES

Research Article

Cite This: ACS Appl. Mater. Interfaces 2019, 11, 40214−40221

www.acsami.org

Material Design of New p-Type Tin Oxyselenide Semiconductor through Valence Band Engineering and Its Device Application

Taikyu Kim,[†] Baekeun Yoo,[†] Yong Youn,[‡] Miso Lee,[‡] Aeran Song,[§] Kwun-Bum Chung,[§] Seungwu Han,[‡] and Jae Kyeong Jeong*[,†]

[†]Department of Electronic Engineering, Hanyang University, Seoul 04763, Korea

[‡]Department of Materials Science and Engineering and Research Institute of Advanced Materals, Seoul National University, Seoul 08826, Korea

[§]Division of Physics and Semiconductor Science, Dongguk University, Seoul 04620, Korea

Supporting Information

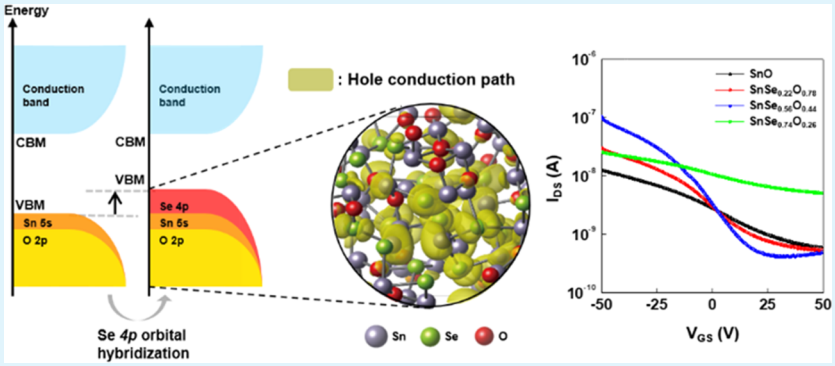

ABSTRACT: This paper reports a new p-type tin oxyselenide (SnSeO), which was designed with the concept that the valence band edge from O 2p orbitals in the majority of metal oxides becomes delocalized by hybridizing Se 4p and Sn 5s orbitals. As the Se loading increased, the SnSeO film structures were transformed from tetragonal SnO to orthorhombic SnSe, which was accompanied by an increase in the amorphous phase portion and smooth morphologies. The $SnSe_{0.56}O_{0.44}$ film annealed at 300 °C exhibited the highest Hall mobility (μ_{Hall}), 15.0 cm^2 $(V\ s)^{-1}$, and hole carrier density (n_h), 1.2×10^{17} cm^{-3}. The remarkable electrical performance was explained by the low hole effective mass, which was calculated by a first principle calculation. Indeed, the fabricated field-effect transistor (FET) with a p-channel $SnSe_{0.56}O_{0.44}$ film showed the high field-effect mobility of 5.9 cm^2 $(V\ s)^{-1}$ and an $I_{ON/OFF}$ ratio of 3×10^2. This work demonstrates that anion alloy-based hybridization provides a facile route to the realization of a high-performance p-channel FET and complementary devices.

KEYWORDS: *p-type inorganic semiconductor, Sn−Se−O, valence band engineering, high mobility, thermal stability*

INTRODUCTION

In 2004, a new class of n-type amorphous indium−gallium−zinc oxide (a-IGZO) semiconductors was discovered in which the n-channel a-IGZO field-effect transistors (FETs) have excellent electrical and optical properties to replace the conventional amorphous Si-based FETs.[1] The development of n-type amorphous oxide semiconductors (AOSs) has attracted much interest because it is applicable to various electronics, such as semiconductor, flat-panel displays, solar cells, electronic paper, and light-emitting diodes. The traditional two-dimensional scaling of Si semiconductor predicted by Moore's law faces the fundamental physical limitation. Monolithic three-dimensional (3D) integration provides a promising pathway to extend the semiconductor roadmap beyond complementary metal oxide semiconductors (CMOS) technology.[2] Indeed, the integration of several memory circuits on top of CMOS logic circuit has been demonstrated with the improvement in terms of speed, power, and performance.[3] This monolithic heterogeneous integration, however, requires a low-temperature process (≤400 °C) because (i) a high temperature negatively affects the performance of underlying CMOS logic devices and (ii) 3D stacking of nonvolatile memory, selector, and driver array favors the low-temperature process.[4,5] The p-type oxide semiconductor as well as n-type IGZO can be used as the essential ingredient for the memory selector and driver due to their low-temperature compatibility and good processability.[6,7] However, in the case of p-type oxide semiconductors, the valence band (VB) edge acts as a hole conduction path that is mainly formed of anisotropic and localized oxygen 2p orbitals, thereby resulting in a large hole

Received: July 11, 2019
Accepted: October 2, 2019
Published: October 2, 2019

DOI: 10.1021/acsami.9b12186
ACS Appl. Mater. Interfaces 2019, 11, 40214−40221

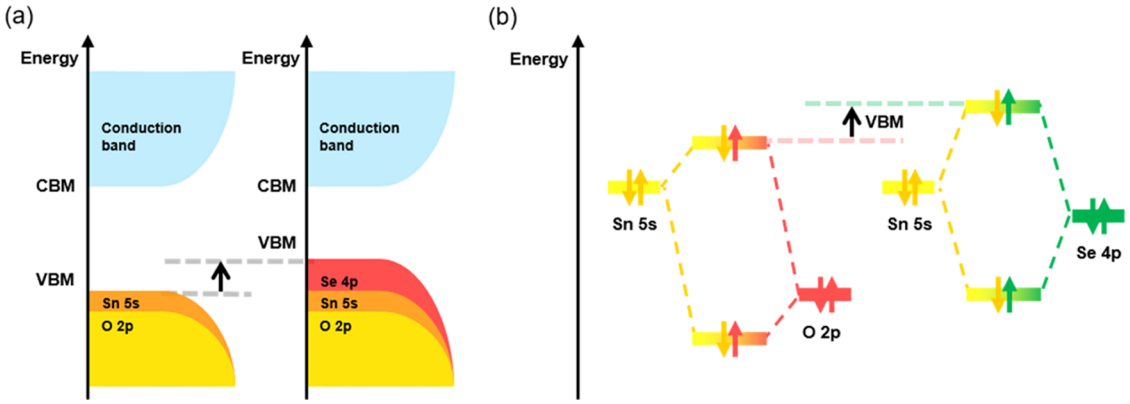

Figure 1. (a) Valence band extension through a combination of the selenium 4p orbital. (b) Schematic orbital hybridization of the valence band.

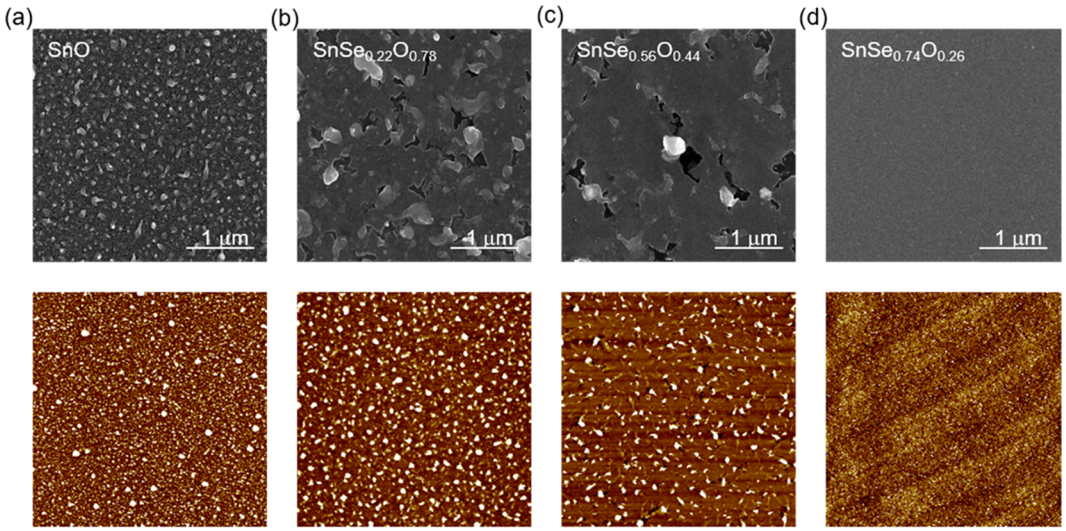

Figure 2. Evolution in surface morphologies: scanning electron microscopy (SEM) and atomic force microscopy (AFM) images of the $SnSe_xO_{1-x}$ films with (a) $x = 0$, (b) $x = 0.22$, (c) $x = 0.56$, and (d) $x = 0.74$.

effective mass (m_h*) and poor transport characteristics. Moreover, the p-type dopability is limited by the high formation energy of point defects, such as cation vacancies, that create free holes. To make matters worse, the facile generation of native hole killers, such as anion vacancies, strongly compensates for the possible p-type doping.[8,9] Therefore, it is challenging to develop the p-type oxide semiconductors that are capable of realizing high-performance FETs. In 1997, the seminal work performed by Kawazoe and co-workers demonstrated a p-type electrical conduction in transparent $CuAlO_2$ films.[10] Since then, the delafossite family $CuMO_2$ (M = Al, Ga, In, Y, Sc, La, etc.) and cuprous oxide (Cu_2O) have been studied intensively for the p-type oxide semiconductor and related FET devices.[11−17] The hybridization of copper 3d and oxygen 2p orbitals mitigated the localization of the VB edge. However, significant VB edge tail states still exist for the delafossite materials, which results in low hole mobility and/or an unsuitable hole carrier density. Additionally, other p-type oxide semiconductors, such as tin monoxide (SnO) and nickel oxide (NiO_x), have been studied by several groups.[18−31] Among them, SnO has been considered to be the most promising p-type oxide semiconductor, in which the pseudo-closed ns^2 orbital of Sn^{2+} ions near the VB edge provides a pathway for hole carriers. However, the p-type SnO is a metastable phase that easily transforms to n-type SnO_2 by a local disproportionate reaction, which is responsible for an extremely narrow thermodynamic stability of accurate p-type phase in terms of oxygen partial pressure, chamber pressure, and postannealing temperature. Indeed, the fabricated p-type SnO FETs annealed at elevated temperature (>250 °C) tend to suffer from seriously deteriorated mobility and/or loss of p-channel property, limiting their widespread application. Therefore, the inferior thermal instability of the p-type SnO compared with that of the n-type SnO_2 and the polycrystalline nature of the SnO film are great concern for large-area scalability and uniform electrical performance.

In this study, we report a new p-type semiconducting tin oxyselenide (SnSeO) with promising electrical performances, which was fabricated using reactive sputtering method. The tin cation (Sn^{2+}) was selected as the primary origin of p-type characteristics. Here, the novel concept of anion hybridization is introduced for the first time, where oxygen anion sites are alloyed by selenium anion. The oxyselenide was chosen because (1) the energy level of the selenium 4p orbital lies on that of the oxygen 2p orbital and (2) its ionic radius is larger compared with that of the oxygen ion. Therefore, the VB edge would consist of near-isotropic hybrid orbitals of Se 4p, Sn 5s, and O 2p orbitals, thus resulting in the low hole effective mass (m_h*) and enhanced carrier mobility in the formed SnSeO films. Our concept design involving valence band engineering

DOI: 10.1021/acsami.9b12186
ACS Appl. Mater. Interfaces 2019, 11, 40214−40221

is illustrated in Figure 1. Furthermore, the Se alloying into SnO substance can widen the thermal stability of p-type SnSeO film up to 350 °C, which can be explained by the mitigation of disproportional reaction of SnO to Sn and n-type SnO_2 by strong ionic bond between Sn^{2+} and Se^{2-}. Beside, the combination of selenium ions would partially inhibit the formation of crystallization-induced grain boundary defects, which is one of the critical limitations of SnO in terms of electrical uniformity and the leakage of current characteristics.

RESULTS AND DISCUSSION

Characterization depending on the Selenium Fraction. Figure 2a–d shows the evolution of the surface morphologies of $SnSe_xO_{1-x}$ films with different Se fractions. All $SnSe_xO_{1-x}$ (x = 0, 0.22, 0.56, 0.74) films were annealed at 300 °C under vacuum atmosphere to verify the enhanced thermal stability of p-type SnSeO films at elevated processing temperature. The control SnO film had a rather rough morphology, which consisted of many protruded clusters in the continuous matrix film (Figure 2a). In this study, the control SnO film was grown by reactive sputtering under an oxygen-poor condition. The agglomeration of the excess Sn cluster in the as-deposited film toward the film surface and subsequent oxidation during thermal annealing can result in this kind of morphology.[22,24] This postulation can be confirmed by the fact that the annealed SnO films prepared at higher oxygen partial pressure contain less protruded clusters (Figure S1, Supporting Information). Thus, the excess metallic Sn fraction incorporated in the as-deposited SnO film is interpreted to accelerate the nuclei formation of protrusion. Notably, the density of these clusters for the SnSeO films was reduced with the increasing Se fraction, which led to smoother morphologies: the root-mean-square (rms) values for the SnO and $SnSe_{0.56}O_{0.44}$ films (Se fraction = 25 atom %) were 36.4 and 15.6 nm, respectively (Table 1). Our interesting finding is

Table 1. Variations in the Surface Roughness, Hole Carrier Concentration and Mobility of $SnSe_xO_{1-x}$ Films Depending on the Content of Selenium annealed at 300 °C[a]

	SnO	$SnSe_{0.22}O_{0.78}$	$SnSe_{0.56}O_{0.44}$	$SnSe_{0.74}O_{0.26}$
surface roughness (nm)	36.4	32.2	15.6	0.6
n_h (cm^{-3})		5.6×10^{16}	1.2×10^{17}	4.7×10^{16}
μ_{Hall} (cm^2 $(V\ s)^{-1}$)		6.2 ± 2	15.0 ± 4	13.3 ± 2

[a]Hall effect for the control SnO films annealed at 300 °c could not be measured due to its high resistivity

that metallic Sn fraction in the annealed SnSeO films decreased with increasing Se loading, which will be discussed in X-ray photoelectron spectroscopy (XPS) analysis. Therefore, the improved morphology of SnSeO films should be explained by the diminished metallic Sn fraction in the as-deposited film where the incorporated Se ions such as Se^{2-} during the deposition of SnSeO film and/or postannealing process can effectively either oxidize the neutral Sn species or mitigate the agglomeration of excess Sn clusters. The featureless and extremely smooth morphology (rms value of 0.6 nm) was obtained for the $SnSe_{0.74}O_{0.26}$ film with the highest Se fraction, which suggested an entirely different microstructure.

Figure 3a shows the X-ray diffraction (XRD) patterns of the $SnSe_xO_{1-x}$ thin films with different contents of selenium. The SnO film annealed at 300 °C has multiple discernible peaks at

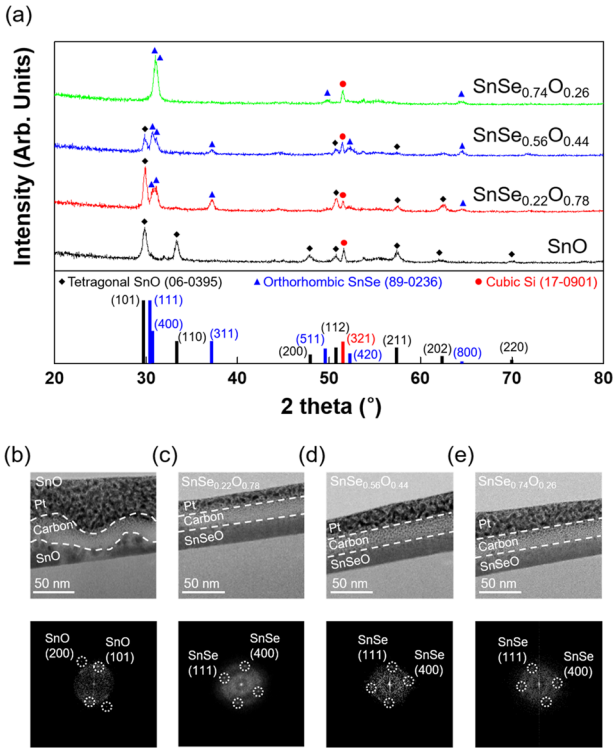

Figure 3. (a) XRD patterns of thin films depending on the content of selenium. The TEM cross-sectional image and SAD pattern of each thin film: (b) SnO, (c) $SnSe_{0.22}O_{0.78}$, (d) $SnSe_{0.56}O_{0.44}$, and (e) $SnSe_{0.74}O_{0.26}$.

approximately 29.9, 33.3, 57.4, and 69.9°, as shown in Figure 3a. Considering that crystalline SnO has a tetragonal symmetry (space group P4/nmm, No. 129), these peaks can be assigned to the (101), (110), (200), (112), and (211) reflections. The small peak near 52° was identified as the (321) reflection of cubic Si coming from the Si substrate. The $SnSe_{0.22}O_{0.78}$ film that was fabricated at the sputtering condition (the target powers of Sn and SnSe were 50 and 30 W, respectively) had new peaks at 30.4, 30.9, and 37.6°, which can be assigned to the (111), (400), and (311) reflections of SnSe (orthorhombic system, space group *Pnma*, No. 62), respectively. This result suggests that the microstructure of the synthesized film consists of derivatives of polycrystalline SnO and SnSe phases. Interestingly, the (111) and (400) peaks of the SnSe phase grew with the increasing Se fraction, whereas the peaks related to the crystal SnO grains diminished or disappeared, as shown in Figure 3a. Thus, the $SnSe_{0.74}O_{0.26}$ film with the highest Se fraction had only crystalline SnSe-related peaks. Because the amorphous phases included in nanoscale SnSeO films cannot be detected in XRD patterns, plan-view and cross-sectional transmission electron microscopy (XTEM) analyses were performed. The XTEM image of the SnO film clearly showed a very rough morphology, which was consistent with the scanning electron microscopy (SEM) and atomic force microscopy (AFM) results. The selected area diffraction pattern indicated the formation of the crystalline SnO phase. In contrast, the SnSeO films with the increasing Se fraction had smoother interfaces and uniformities in terms of physical thickness (Figure 3c–e). Simultaneously, amorphous phase regions with significant portions were observed for the $SnSe_{0.56}O_{0.44}$ film: the volume fraction of the amorphous region for the entire $SnSe_{0.56}O_{0.44}$ film was estimated to be 60–

DOI: 10.1021/acsami.9b12186
ACS Appl. Mater. Interfaces 2019, 11, 40214–40221

80% (Figure S2, Supporting Information). However, the $SnSe_{0.74}O_{0.26}$ film with the highest Se fraction was completely crystallized, which is consistent with the preferential orientation of the (111) and (400) SnSe phases. The extremely smooth morphology of the $SnSe_{0.74}O_{0.26}$ film should be related to its orthorhombic SnSe-derived microstructure.

The Hall effect for the $SnSe_xO_{1-x}$ thin films with different Se fractions was characterized to assess the feasibility of the p-type semiconductor. The positive Hall coefficient was observed for all $SnSe_xO_{1-x}$ films annealed at 300 °C, thus indicating the p-type semiconducting behavior. The Hall effect measurement for the control SnO film annealed at 300 °C under vacuum atmosphere (2.0×10^{-3} Torr) could not be done due to its high resistance. It is noted, however, that the 30 nm thick SnO film annealed at 200 °C under air atmosphere exhibited the Hall mobility (μ_{Hall}) of 3.9 cm^2 $(V\ s)^{-1}$ and hole carrier density (n_h) of 3.0×10^{18} cm^{-3}, representing the typical p-type SnO film. The increase in the resistivity of control SnO film at 300 °C can be attributed to the carrier compensation effect due to the overoxidation from the p-type SnO to n-type SnO_2. Up to the Se fraction of 25 atom %, the μ_{Hall} of the SnSeO films annealed at 300 °C was enhanced by the increase in the n_h of the SnSeO films, as shown in Table 1. Thus, the $SnSe_{0.56}O_{0.44}$ film exhibited the highest μ_{Hall} of 15.0 cm^2 $(V\ s)^{-1}$ and n_h of 1.2×10^{17} cm^{-3}. In contrast, the $SnSe_{0.74}O_{0.26}$ had the slightly reduced μ_{Hall} of 13.3 cm^2 $(V\ s)^{-1}$ and n_h of 4.7×10^{16} cm^{-3}, which suggested a different film formation. Interestingly, the μ_{Hall} values for all $SnSe_xO_{1-x}$ films, irrespective of the Se fraction, tend to increase with the increasing n_h (Table 1 and Table S1, Supporting Information). The exact mechanism is not yet known, but a similar percolation conduction is well-known for conventional transparent amorphous oxide semiconductors (TAOSs).[32]

The origin of high mobility for the $SnSe_xO_{1-x}$ films was studied on basis of the density functional theory (DFT) calculation. Three amorphous structures with the compositional ratio of 2:1:1 (Sn/Se/O) were generated following the conventional melt-quench molecular dynamics simulation.[33] (See method section for details.) In Figure 4a, the

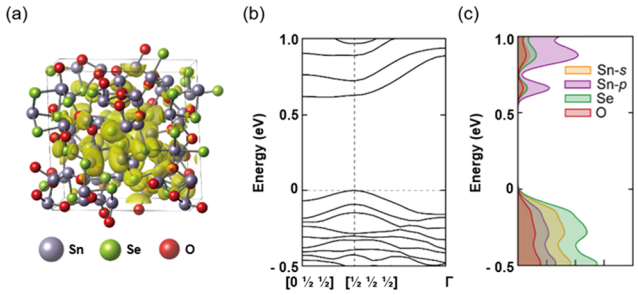

Figure 4. (a) Atomic configuration of a-SnSeO with the ratio of 2:1:1 (Sn/Se/O) and the charge distribution at the VB edge. (b) and (c) Band structure and density of the states of a-SnSeO, respectively.

coordination numbers of each atom in the amorphous structures were approximately 3, such as the crystal SnSe in which the Sn exists as Sn^{2+}.[34] Additionally, there was no preference for a specific anion around Sn. In the band structure in Figure 4b, a dispersive valence band was observed, which was similar to the conduction band of IGZO. Therefore, the harmonic averaged hole effective mass (m_h^* = 0.58, 0.93, 1.99 m_e over various amorphous models) was low enough to be comparable to that of the crystal SnO (m_h^* = 1.25 m_e), in spite of the structural disorder.[35] The low effective mass was caused by the hybridization of metal *s* and the anion p orbital at the valence band, as shown in Figure 4c, which is consistent with the conduction band character of IGZO.[1] The charge distribution in Figure 4a also shows that the valence band mainly consists of the Sn-5s and Se-4p hybridized orbitals.

To obtain further insight into the Se fraction-dependent electrical performance, the chemical states of Sn, Se, and O in the $SnSe_xO_{1-x}$ (x = 0.22, 0.56, and 0.74) thin films were examined using XPS. Figure 5a−d shows the Sn $3d_{5/2}$ peaks of the XP spectra for the channel layers depending on the selenium fraction annealed at 300 °C. The binding energy states of the Sn atoms with three different oxidation numbers (Sn^0, Sn^{2+}, and Sn^{4+}) correspond to the peaks at approximately 486.0, 486.9, and 487.4 eV, respectively.[19] First, the control 300 °C-annealed SnO film had a significant portion (∼36.1%) of Sn^{4+}, which corroborates its high electrical resistivity as discussed in the Hall effect analysis. With the Se fraction increasing up to 25 atom %, the Sn^{2+}- and Sn^{4+}-related peaks grew, whereas the metallic Sn (Sn^0)-related peak diminished. The relative peak areas of Sn^{2+} and Sn^{4+} for the $SnSe_{0.56}O_{0.44}$ films increased from 49.1 and 36.1% (SnO film) to 53.2 and 39.1%, respectively. In contrast, the Sn^0-related peak for the $SnSe_{0.56}O_{0.44}$ films decreased from 14.8 (SnO film) to 7.8%. The enhanced oxidation of metallic Sn in $SnSe_xO_{1-x}$ (x = 0.22, 0.56) films compared with the reference SnO film can be explained by the efficient formation of the ionic Sn−Se bond during vacuum annealing, which was also confirmed by the Se 3d XP spectra (Figure S3, Supporting Information). The microstructural changes of $SnSe_xO_{1-x}$ film from the tetragonal SnO phase to orthorhombic SnSe-derivative phase and its improved morphology are consistent with the reduction in the metallic Sn content. In the p-type SnO, the same trace of the metallic Sn component boosts the hole mobility by promoting delocalization in the VB edge.[18] Therefore, the enhancement in the hole carrier mobility for $SnSe_xO_{1-x}$ with the increasing Se fraction cannot be attributed to the reduction in the metallic Sn unlike the SnO. The modification in the relative band structure of SnSeO films can be seen in the XPS VB profiles, as shown in Figure 5e. The VB edges of the $SnSe_xO_{1-x}$ (x = 0.22, 0.56) films were extended compared with those of the control SnO sample, which indicated that the Se 4p orbital significantly contributed to the delocalization of the VB edge. However, the $SnSe_{0.74}O_{0.26}$ film had the largest Sn^{4+} (40.7%) and smallest Sn^{2+} (48.7%) portions among SnSeO films. It can be conjectured that the excess Se loading during co-sputtering promotes the overoxidation of Sn^0 and Sn^{2+}, leading to the formation of $SnSe_2$ (Figure S3, Supporting Information), which should be related to the complete disappearance of the protrusion for the $SnSe_{0.74}O_{0.26}$ film.

In addition, the optical transmittance of the 30 nm thick $SnSe_xO_{1-x}$ (x = 0, 0.22, 0.56, 0.74) films annealed at 300 °C was examined through UV−visible spectroscopy (UV−vis). The average transmittance in the visible region (400−700 nm) was reduced from 61% to 6% with the increasing Se fraction (Figure S4, Supporting Information). The direct band gap (E_g) of the SnSeO films, which depended on the Se fraction, was extracted using the Tauc plot. The E_g of SnO was 2.8 eV, which is consistent with that reported for the SnO film in the literature.[18] Expectedly, the E_g values of $SnSe_xO_{1-x}$ (x = 0.22, 0.56, 0.74) monotonously decreased to 2.0, 1.93, and 1.67 eV, respectively, with the increasing Se fraction. The E_g value (1.67

DOI: 10.1021/acsami.9b12186
ACS Appl. Mater. Interfaces 2019, 11, 40214−40221

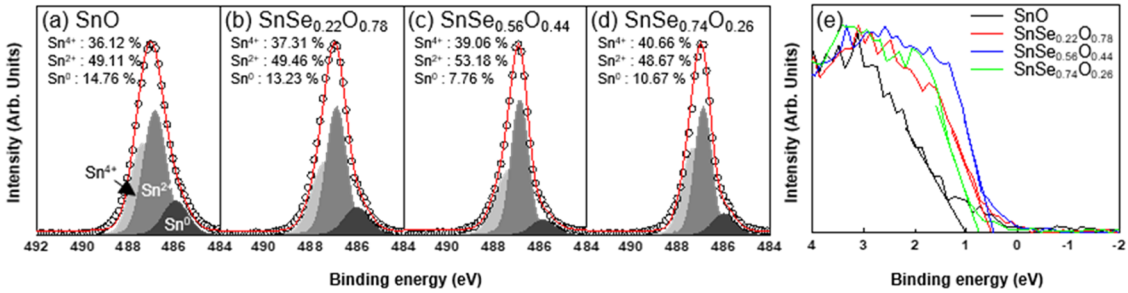

Figure 5. XPS spectra of Sn $3d_{5/2}$ of SnSeO thin films depending on the content of selenium: (a) SnO, (b) $SnSe_{0.22}O_{0.78}$, (c) $SnSe_{0.56}O_{0.44}$, and (d) $SnSe_{0.74}O_{0.26}$. (e) VB edge of SnSeO with different contents of selenium.

eV) for the $SnSe_{0.74}O_{0.26}$ film is comparable to that of the crystalline $SnSe_2$, which was quite consistent with the microstructural change in Figure 2.[36] Based on the VB spectra and the extracted E_g values, the schematic energy band diagram for the $SnSe_xO_{1-x}$ films was constructed (Figure S5, Supporting Information). The VB offset (ΔE_{VB}) between the VB edge and the Fermi energy level (E_F) decreased from 0.94 eV (SnO) to 0.45 eV ($SnSn_{0.56}O_{0.44}$), which may partially constitute the reason for the increase in the free hole carrier density (n_h). In contrast, the ΔE_{VB} value of $SnSe_{0.74}O_{0.26}$ increased to 0.73 eV, which can be corroborated by its reduced n_h value (Table 1).

Effect of the Selenium on the Electrical Characteristics. Next, the effect of selenium loading on the performance of the $SnSe_xO_{1-x}$ FETs was examined. Figure 6a,b shows the

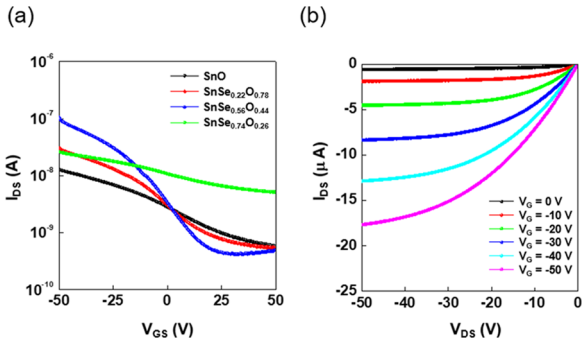

Figure 6. (a) Transfer characteristics of SnSeO FETs depending on the selenium loading at $V_{DS} = -0.1$ V. (b) Output characteristics of $SnSe_{0.56}O_{0.44}$ FETs containing the 25 atom % selenium.

transfer characteristics of the SnSeO FETs annealed at 300 °C with the different contents of selenium and output characteristics of the $SnSe_{0.56}O_{0.44}$ FET, respectively. All FETs exhibited clear p-channel conduction-based switching characteristics. The control SnO FETs annealed at 300 °C without selenium suffered from a low μ_{FE} (0.23 cm^2 $(V\ s)^{-1}$) and poor $I_{ON/OFF}$ ratio (2×10^1). The transporting and switching characteristics of the $SnSe_xO_{1-x}$ FETs were enhanced up to $x = 0.56$ by the increasing Se fraction through valence band engineering. Therefore, the substantial improvements in the terms of the μ_{FE} (5.9 cm^2 $(V\ s)^{-1}$) and $I_{ON/OFF}$ ratio (3×10^2) were observed for the $SnSe_{0.56}O_{0.44}$ FETs (also see Figure S6, Supporting Information). It is also noted that the electrical performance of the $SnSe_xO_{1-x}$ thin films and their FETs with Se fraction near $x = 0.56$ were independent of the Se fraction, which ranged from 0.46 to 0.62: the n_h, μ_{FE} and $I_{ON/OFF}$ ratio were 0.8−1.2 × 10^{17} cm^{-3}, 4.0−5.9 cm^2 $(V\ s)^{-1}$, and 1−3 × 10^2, respectively (Figure S7 and Table S1, Supporting Information). However, a further increase in the Se fraction deteriorated the μ_{FE} and $I_{ON/OFF}$ ratio to 0.47 cm^2 $(V\ s)^{-1}$ and 5×10^0, respectively, for the resulting $SnSe_{0.74}O_{0.26}$ devices (Figure 6a). It would be interesting to investigate the effect of selenium loading on the thermal stability of the transfer characteristics of p-type SnSeO FETs. Generally, the highest mobility of the p-type SnO FETs have been observed for the low-temperature annealing (≤200 °C) condition (Table S2 and Figure S8, Supporting Information). The SnO FETs annealed at 200 °C under air atmosphere, in this study, showed the μ_{FE} of 1.0 cm^2 $(V\ s)^{-1}$ and $I_{ON/OFF}$ ratio of 1.0×10^3 (Figure S9, Supporting Information), which are better than those (0.23 cm^2 $(V\ s)^{-1}$ and 2×10^1) of the control SnO FET annealed at 300 °C under vacuum atmosphere (Figure 6). However, this p-type characteristic disappeared for the SnO FETs when the annealing temperature increased to 250 and 300 °C under air atmosphere (Figure S9, Supporting Information). Instead, the weak n-type behavior was observed, which is a well-known thermal instability issue for the SnO FETs. It can be attributed to the facile oxidation from the metastable Sn^{2+} phase to the stable Sn^{4+} phase at elevated temperatures (≥250 °C) under air atmosphere. In contrast, the $SnSe_{0.56}O_{0.44}$ thin films annealed at 350 °C had the average n_h of 3.4×10^{16} cm^{-3} and μ_{Hall} of 12.0 cm^2 $(V\ s)^{-1}$, and the corresponding FETs exhibited a strong thermal stability with the same p-type characteristics (Figure S10, Supporting Information). This entirely different behavior can be related to the dominant existence of orthorhombic SnSe phase, as discussed in the XRD analysis and peculiar modification near the top of VB by contribution of Se 4p orbital. The result suggests that the overall network of $SnSe_{0.56}O_{0.44}$ film is a derivative of the SnSe phase where O^{2-} ion may substitute the anion site of Se. It is also noted that the Hall mobility of 15.0 cm^2 $(V\ s)^{-1}$ obtained for the $SnSe_{0.56}O_{0.44}$ film corresponds to the state-of-the-art metric for any SnO film reported up to now (Table S2 and Figure S8, Supporting Information). Rather lower field-effect mobility of 5.9 cm^2 $(V\ s)^{-1}$ for $SnSe_{0.56}O_{0.44}$ FETs can be improved by further engineering such as usage of high-k dielectric, low Ohmic contact schematic, Fermi level unpinning, suitable passivation, etc. Combining the p-type $SnSe_{0.56}O_{0.44}$ TFT with a n-type IGZO TFT, which exhibits a great device performance with the μ_{FE} of 19.3 cm^2 $(V\ s)^{-1}$ and $I_{ON/OFF}$ ratio of 10^6 (Figure S11, Supporting Information), we fabricated a CMOS inverter, which reveals a clear signal inversion at a transition voltage near $V_{IN} = V_{DD}/2$ and the corresponding intrinsic gain shows the highest value of 15.7 at the applied V_{DD} of 30 V as shown in Figure 7.

DOI: 10.1021/acsami.9b12186
ACS Appl. Mater. Interfaces 2019, 11, 40214−40221

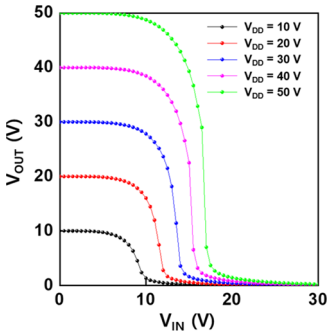

Figure 7. Output characteristics of the complementary metal oxide semiconductors (CMOS) using n-type IGZO and p-type $SnSe_{0.56}O_{0.44}$.

Finally, the operation stress-induced instabilities of the $SnSe_xO_{1-x}$ (x = 0, 0.22, 0.56, 0.74) FETs annealed at 300 °C were examined by measuring the $I_{DS}-V_{GS}$ curves in the double-sweep gate voltage mode (Figure S12, Supporting Information). The control SnO FET suffered from the huge counterclockwise hysteresis (ΔV_{TH}) of approximately 19.6 V, which can be attributed to the hole trapping in the bulk trap defects and/or the interface states within the channel layer. The hysteresis phenomenon diminished with increasing Se loading: the amount of hysteresis (ΔV_{TH}) for the $SnSe_{0.22}O_{0.78}$ and $SnSe_{0.56}O_{0.44}$ FETs were ∼15.4 and 13.8 V, respectively, indicating that the Se loading is effective to reduce the bulk/interface trap states. Indeed, nearly hysteresis-free behavior was observed for the $SnSe_{0.74}O_{0.26}$ FETs.

CONCLUSIONS

In summary, this study demonstrated a new p-type SnSeO film based on the hybridization of the anion Se 4p and O 2p orbital. The evolution in the structural, chemical, and electrical properties of SnSeO films with different Se fractions was investigated. The synthesized $SnSe_{0.56}O_{0.44}$ films annealed at 300 °C exhibited a high Hall mobility of 15.0 cm^2 $(V\ s)^{-1}$ and a reasonable n_h of 1.2×10^{17} cm^{-3}, which was attributed to its low hole effective mass and dopability confirmed by the DFT calculation. The synergic overlap approach of the Se 4p, Sn 5s, and O 2p orbitals can pave a promising pathway for hole carriers through the delocalization of the VB edge. Also, the strong ionic bond between Sn^{2+} and Se^{2-} mitigates the disproportional reaction of SnO, leading to the superb thermal stability of the p-channel SnSeO FETs up to 350 °C. Therefore, this wider process window of the p-type SnSeO substance in terms of thermal budget would be helpful for a heterogeneous integration of CMOS TFTs with a stackable memory on the CMOS logic device (a memory-in-logic system) where it works as an advanced memristor, switcher, amplifier, and inverter.

METHODS

Experimental Procedure. Bottom-gate, staggered-type FETs were fabricated on a thermally oxidized SiO_2 (100 nm)/heavily doped n^+-Si substrates where the conductive substrate acts as a gate electrode. The 30 nm thick $SnSe_xO_{1-x}$ films with x = 0, 0.22, 0.56 and 0.74 were grown by a reactive magnetron co-sputtering using a metal Sn target (5 N purity, iTASCO, Seoul, Korea) and ceramic SnSe target (4 N purity, iTASCO, Seoul, Korea) at room temperature. The co-sputtering was carried out at gas flow rates of Ar (30 sccm) and O_2 (0.4 sccm), and the chamber pressure was 2 mTorr. The input DC power of the metal Sn target was fixed at 50 W, whereas that of the SnSe target varied from 0 to 150 W. The anion fraction of Se in the SnSeO films was controlled by adjusting the power of the SnSe target. The ITO source/drain (S/D) electrode (180 nm) were formed by sputtering in the same chamber. The patterning of the channel and the S/D was performed using a metal shadow mask. The channel width (W) and length (L) of the fabricated FETs were 100 and 150 μm, respectively. The samples were subjected to thermal annealing at 200, 250, 300, and 350 °C for 1 h under vacuum atmosphere (2.0×10^{-3} Torr) to prevent selenium in the thin film from being volatilized and replaced with oxygen.

Characterization. The chemical states and compositions of the SnSeO films were analyzed by X-ray photoelectron spectroscopy (XPS, Veresprobe II, Ulvac-phi). To avoid confusion from the contamination and the possible oxidation of the film surface during the air exposure before the XPS analysis, the thin surface layer (∼3 nm) was in situ etched using an accelerated (1 kV) Ar^+ ion before the spectrum acquisition. The Sn $3d_{5/2}$ and Se 3d3d peak areas were integrated and converted into the atomic ratio using the sensitivity factor of XPS equipment for the given SnSeO films. The valence band offsets between the VB edge and E_F were extracted using the maximum XPS-measured valence-band spectra. The transmittances of the SnSeO films on the glass substrate were confirmed using UV−vis spectroscopy (UV−vis, V-770, JASCO). The crystalline structures of the SnSeO films were examined by X-ray diffraction (XRD, X'Pert-PRO MRD, Phillips) and transmission electron microscopy (TEM, JEM 2100F, JEOL). The surface morphology was observed by field-emission scanning electron microscopy (SEM, NOVA NANO SEM 450, FEI) and atomic force microscopy (AFM, XE-100, Parksystems). The carrier type, concentration and mobility of the SnSeO films were characterized by the Hall effect measurement (HMS-5000, Ecopia) with the van der Pauw configuration at room temperature. For the Hall effect evaluation, the 30 nm thick SnO and SnSeO films were deposited on the 100 nm thick SiO_2/Si substrate, and the sputtered ITO electrodes (180 nm) were used for Ohmic contact. The electrical characteristics of the SnSeO FETs were measured in air by an $I-V$ meter (Keithley 2636, Keithley) at room temperature.

Calculation. We performed the density functional theory calculation using Vienna Ab initio Simulation Package.[37] The generalized gradient approximation (GGA) was employed for the exchange−correlation functional.[38] We used 400 eV as the energy cutoff of the plane wave basis and the Γ point only for k-point sampling. The amorphous structures of the SnSeO containing 108 atoms were modeled using the melt-quenching protocol. We performed premelting for 1 ps at 5000 K, melting for 10 ps at 1500 K, and quenching to 300 K with a constant cooling rate of −100 K ps^{-1}. Then, the final configurations were obtained by full relaxation of the cell parameters and atomic positions. For the statistical average, we modeled three amorphous samples using the same protocol.

ASSOCIATED CONTENT

Supporting Information

The Supporting Information is available free of charge on the ACS Publications website at DOI: 10.1021/acsami.9b12186.

Cross-sectional SEM images of the SnO film with different oxygen partial pressure; plan-view TEM image of the $SnSe_{0.56}O_{0.44}$ film; XPS analysis of the Se 3d peak; transmittance and band alignment of the $SnSe_xO_{1-x}$ films; $I_{DS}-V_{GS}$ curve and V_{GS}-dependent field-effect mobility variation of the $SnSe_{0.56}O_{0.44}$ FETs; rlectrical characteristics of the $SnSe_xO_{1-x}$ films and their FETs near x = 0.56; Comparison with several important p-type materials recently reported; Comparison of thermal stability between the SnO and $SnSe_{0.56}O_{0.44}$ FETs; transfer characteristics of the n-type IGZO FETs for CMOS inverter; $I_{DS}-V_{GS}$ curves of the $SnSe_xO_{1-x}$ FETs in double-sweep gate voltage mode; and references (PDF)

DOI: 10.1021/acsami.9b12186
ACS Appl. Mater. Interfaces 2019, 11, 40214−40221

AUTHOR INFORMATION

Corresponding Author

*E-mail: jkjeong1@hanyang.ac.kr.

ORCID

Yong Youn: 0000-0003-3924-1373

Jae Kyeong Jeong: 0000-0003-3857-1039

Notes

The authors declare no competing financial interest.

ACKNOWLEDGMENTS

This work was supported by Samsung Research Funding Center for Future Technology through Samsung Electronics.

REFERENCES

(1) Nomura, K.; Ohta, H.; Takgi, A.; Kamiya, T.; Hirano, M.; Hosono, H. Room-Temperature Fabrication of Transparent Flexible Thin-Film Transistors Using Amorphous Oxide Semiconductors. *Nature* **2004**, *432*, 488−492.

(2) 2017 International Roadmap for Devices and Systems (IRDS) − More Moore, 2018, https://irds.ieee.org/images/files/pdf/2017/2017IRDS_MM.pdf.

(3) Shulaker, M. M.; Hills, G.; Park, R. S.; Howe, R. T.; Saraswat, K.; Wong, H.-S. P.; Mitra, S. Three-Dimensional Integration of Nanotechnologies for Computing and Data Storage on a Single Chip. *Nature* **2017**, *547*, 74−78.

(4) Aluguri, R.; Tseng, T.-Y. Overview of Selector Devices for 3-D Stackable Cross Point RRAM Arrays. *IEEE. J. Electron Devices Soc.* **2016**, *4*, 294−306.

(5) Lee, M.-J.; Kim, S. I.; Lee, C. B.; Yin, H.; Ahn, S.-E.; Kang, B. S.; Kim, K. H.; Park, J. C.; Kim, C. J.; Song, I.; Kim, S. W.; Stefanovich, G.; Lee, J. H.; Chung, S. J.; Kim, Y. H.; Park, Y. Low-Temperature-Grown Transition Metal Oxide Based Storage Materials and Oxide Transistors for High-Density Non-Volatile Memory. *Adv. Funct. Mater.* **2009**, *19*, 1587−1593.

(6) Sunamura, H.; Kaneko, K.; Furutake, N.; Saito, S.; Narihiro, M.; Ikarachi, N.; Hane, M.; Hayashi, Y. *High-Voltage Complementary BEOL-FETs on Cu Interconnects Using n-Type IGZO and p-Type SnO Dual Oxide Semiconductor Channels*, 2013 Symposium on VLSI Technology; IEEE: 2013.

(7) Yu, M.-J.; Lin, R.-P.; Chang, Y.-H.; Hou, T.-H. High-Voltage Amorphous InGaZnO TFT With Al_2O_3 High-*k*Dielectric for Low-Temperature Monolithic 3-D Integration. *IEEE Trans. Electron Devices* **2016**, *63*, 3944−3949.

(8) Raebiger, H.; Lany, S.; Zunger, A. Origins of the p-Type Nature and Cation Deficiency in Cu_2O and Related Materials. *Phys. Rev. B* **2007**, *76*, No. 045209.

(9) Togo, A.; Oba, F.; Tanaka, I.; Tatsumi, K. First-Principles Calculations of Native Defects in Tin Monoxide. *Phys. Rev. B* **2006**, *74*, No. 195128.

(10) Kawazoe, H.; Yasukawa, M.; Hyodo, H.; Kurita, M.; Yanagi, H.; Hosono, H. p-Type Electrical Conduction in Transparent Thin Films of $CuAlO_2$. *Nature* **1997**, *389*, 939−942.

(11) Mine, T.; Yanagi, H.; Nomura, K.; Kamiya, T.; Hirano, M.; Hosono, H. Control of Carrier Concentration and Surface Flattening of $CuGaO_2$ Epitaxial Films for a p-Channel Transparent Transistor. *Thin Solid Films* **2008**, *516*, 5790−5794.

(12) Li, B. S.; Akimoto, K.; Shen, A. Growth of Cu_2O Thin Films with High Hole Mobility by Introducing a Low-Temperature Buffer Layer. *J. Cryst. Growth* **2009**, *311*, 1102−1105.

(13) Matsuzaki, K.; Nomura, K.; Yanagi, H.; Kamiya, T.; Hirano, M.; Hosono, H. Epitaxial Growth of High Mobility Cu_2O Thin Films and Application to p-Channel Thin Film Transistor. *Appl. Phys. Lett.* **2008**, *93*, No. 202107.

(14) Fortunato, E.; Figueiredo, V.; Barquinha, P.; Elamurugu, E.; Barros, R.; Goncalves, G.; Park, S. H. K.; Hwang, C. S.; Martins, R. Thin-Film Transistors Based on p-Type Cu_2O Thin Films Produced at Room Temperature. *Appl. Phys. Lett.* **2010**, *96*, No. 192102.

(15) Zou, X.; Fang, G.; Yuan, L.; Li, M.; Guan, W.; Zhao, X. Top-Gate Low-Threshold Voltage p-Cu_2O Thin-Film Transistor Grown on SiO_2/Si Substrate Using a High-*k*HfON Gate Dielectric. *IEEE Electron Device Lett.* **2010**, *31*, 827−829.

(16) Ran, F.-Y.; Taniguti, M.; Hosono, H.; Kamiya, T. Analyses of Surface and Interfacial Layers in Polycrystalline Cu_2O Thin-Film Transistors. *J. Disp. Technol.* **2015**, *11*, 720−724.

(17) Han, S.; Flewitt, A. J. The Origin of the High Off-State Current in p-Type Cu_2O Thin Film Transistors. *IEEE Electron Device Lett.* **2017**, *38*, 1394−1397.

(18) Caraveo-Frescas, J. A.; Nayak, P. K.; Al-Jawhari, H. A.; Granato, D. B.; Schwingenschlogl, U.; Alshareef, H. N. Record Mobility in Transparent p-Type Tin Monoxide Films and Devices by Phase Engineering. *ACS Nano* **2013**, *7*, 5160−5167.

(19) Han, S. J.; Kim, S.; Ahn, J.; Jeong, J. K.; Yang, H.; Kim, H. J. Composition-Dependent Structural and Electrical Properties of p-Type SnO_x Thin Films Prepared by Reactive DC Magnetron Sputtering: Effects of Oxygen Pressure and Heat Treatment. *RSC Adv.* **2016**, *6*, 71757−71766.

(20) Azmi, A.; Lee, J.; Gim, T. J.; Choi, R.; Jeong, J. K. Performance Improvement of p-Channel Tin Monoxide Transistors with a Solution-Processed Zirconium Oxide Gate Dielectric. *IEEE Electron Device Lett.* **2017**, *38*, 1543−1546.

(21) Hung, M. P.; Genoe, J.; Heremans, P.; Steudel, S. Off-Current Reduction in p-Type SnO Thin Film Transistors. *Appl. Phys. Lett.* **2018**, *112*, No. 263502.

(22) Li, Y.; Yang, J.; Qu, Y.; Zhang, J.; Zhou, L.; Yang, Z.; Lin, Z.; Wang, Q.; Song, A.; Xin, Q. Ambipolar SnO_x Thin-Film Transistors Achieved at High Sputtering Power. *Appl. Phys. Lett.* **2018**, *112*, No. 182102.

(23) Shih, C. W.; Chin, A.; Lu, C. F.; Su, W. F. Remarkably High Hole Mobility Metal-Oxide Thin-Film Transistors. *Sci. Rep.* **2018**, *8*, No. 889.

(24) Lee, S. J.; Jang, Y.; Kim, H. J.; Hwang, E. S.; Jeon, S. M.; Kim, J. S.; Moon, T.; Jang, K.-T.; Joo, Y.-C.; Cho, D.-Y.; Hwang, C. S. Composition, Microstructure, and Electrical Performance of Sputtered SnO Thin Films for p-Type Oxide Semiconductor. *ACS Appl. Mater. Interfaces* **2018**, *10*, 3810−3821.

(25) Chen, S. C.; We, C. K.; Kuo, T. Y.; Peng, W. C.; Lin, H. C. Characterization and Properties of NiO Films Produced by RF Magnetron Sputtering with Oxygen Ion Source Assistance. *Thin Solid Films* **2014**, *572*, 51−55.

(26) Wu, C.-C.; Yang, C.-F. Fabricate Heterojunction Diode by Using the Modified Spray Pyrolysis Method to Deposit Nickel−Lithium Oxide on Indium Tin Oxide Substrate. *ACS Appl. Mater. Interfaces* **2013**, *5*, 4996−5001.

(27) Shimotani, H.; Suzuki, H.; Ueno, K.; Kawasaki, M.; Iwasa, Y. p-Type Field-Effect Transistor of NiO with Electric Double-Layer Gating. *Appl. Phys. Lett.* **2008**, *92*, No. 242107.

(28) Jiang, J.; Wang, X.; Zhang, Q.; Li, J.; Zhang, X. X. Thermal Oxidation of Ni Films for p-Type Thin-Film Transistors. *Phys. Chem. Chem. Phys.* **2013**, *15*, 6875−6878.

(29) Matsubara, K.; Huang, S.; Iwamoto, M.; Pan, W. Enhanced Conductivity and Gating Effect of p-Type Li-Doped NiO Nanowires. *Nanoscale* **2014**, *6*, 688−692.

(30) Lin, T.; Li, X.; Jang, J. High Performance p-Type NiO_x Thin-Film Transistor by Sn Doping. *Appl. Phys. Lett.* **2016**, *108*, No. 233503.

(31) Shan, F.; Liu, A.; Zhu, H.; Kong, W.; Liu, J.; Shin, B.; Fortunato, E.; Martins, R.; Liu, G. High-Mobility p-Type NiO_x Thin-Film Transistors Processed at Low Temperatures with Al_2O_3 High-*k* Dielectric. *J. Mater. Chem. C* **2016**, *4*, 9438−9444.

(32) Nomura, K.; Kamiya, T.; Ohta, H.; Ueda, K.; Hirano, M.; Hosono, H. Carrier Transport in Transparent Oxide Semiconductor with Intrinsic Structural Randomness Probed Using Single-Crystalline $InGaO_3(ZnO)_5$ Films. *Appl. Phys. Lett.* **2004**, *85*, 1993.

DOI: 10.1021/acsami.9b12186
ACS Appl. Mater. Interfaces 2019, 11, 40214−40221

(33) Youn, Y.; Kang, Y.; Han, S. An Efficient Method to Generate Amorphous Structures Based on Local Geometry. *Compd. Mater. Sci.* **2014**, *95*, 256−262.
(34) Okazaki, A.; Ueda, I. The Crystal Structure of Stannous Selenide SnSe. *J. Phys. Soc. Jpn.* **1956**, *11*, 470.
(35) Yim, K.; Youn, Y.; Lee, M.; Yoo, D.; Lee, J.; Cho, S. H.; Han, S. Computational Discovery of p-Type Transparent Oxide Semiconductors Using Hydrogen Descriptor. *npj Comput. Mater.* **2018**, *4*, 17.
(36) Mukhokosi, E. P.; Krupanidhi, S. B.; Nanda, K. K. Band Gap Engineering of Hexagonal $SnSe_2$ Nanostructured Thin Films for Infra-Red Photodetection. *Sci. Rep.* **2017**, *7*, No. 15215.
(37) Kresse, G.; Hafner, J. *Ab initio* Molecular Dynamics for Liquid Metals. *Phys. Rev. B* **1993**, *47*, 558.
(38) Perdew, J. P.; Burke, K.; Ernzerhof, M. Generalized Gradient Approximation Made Simple. *Phys. Rev. Lett.* **1996**, *77*, 3865.

DOI: 10.1021/acsami.9b12186
ACS Appl. Mater. Interfaces 2019, 11, 40214−40221